

Planar corner-cut square microcavities: ray optics and FDTD analysis

Chung Yan Fong and Andrew W. Poon

*Department of Electrical and Electronic Engineering, The Hong Kong University of Science and Technology,
Clear Water Bay, Hong Kong SAR, China.*

eeawpoon@ust.hk

Abstract: We analyze corner-cut square microcavities as alternative planar microcavities. Ray tracing shows open-ray orbits that are 90°-rotated can oscillate between each other upon reflections at the 45° corner-cut facets, and have the same sense of circulation. Our two-dimensional finite-difference time-domain simulations suggest that a waveguide-coupled corner-cut square microcavity with an optimum cut size supports traveling-wave resonances with desirable add-drop filter responses. The mode-field pattern evolutions confirm the concept of modal oscillations. By applying Fourier transform on the mode-field patterns, we analyze the modal composition in k-space. The add-drop filter responses can be optimized by fine-tuning the waveguide width.

©2004 Optical Society of America

OCIS codes: (230.5750) Resonators; (260.5740) Resonance

References and links

1. D. Rafizadeh, J. P. Zhang, S. C. Hagness, A. Taflove, K. A. Stair, S. T. Ho and R. C. Tiberio, "Waveguide-coupled AlGaAs/GaAs microcavity ring and disk resonators with high finesse and 21.6-nm free spectral range," *Opt. Lett.* **22**, 1244-1246 (1997).
2. B. E. Little, J. S. Foresi, G. Steinmeyer, E. R. Thoen, S. T. Chu, H. A. Haus, E. P. Ippen, L. C. Kimerling and W. Greene, "Ultra-compact Si-SiO₂ microring resonator optical channel dropping filters," *IEEE Photon. Technol. Lett.* **10**, 549-551 (1998).
3. B. E. Little, S. T. Chu, W. Pan, D. Ripin, T. Kaneko, Y. Kokubun, and E. Ippen, "Vertically coupled glass microring resonator channel dropping filters," *IEEE Photon. Technol. Lett.* **11**, 215-217, (1999).
4. Y. Yanagase, S. Suzuki, Y. Kokubun and S.T. Chu, "Box-like filter response and expansion of FSR by a vertically triple coupled microring resonator filter," *J. Lightwave Technol.* **20**, 1525-1529 (2002).
5. T. Barwicz, M. A. Popovic, P. T. Rakich, M. R. Watts, H. A. Haus, E. P. Ippen, H. I. Smith, "Microring-resonator-based add-drop filters in SiN: fabrication and analysis," *Opt. Express* **12**, 1437-1442, (2004).
6. S. T. Chu, B. E. Little, V. Van, J. V. Hryniewicz, P. P. Absil, F. G. Johnson, D. Gill, O. King, F. Seiferth, M. Trakalo and J. Shantona, "Compact full C-band tunable filters for 50 GHz channel spacing based on high order micro-ring resonators," in proceedings of Optical Fiber Communication Conference (OFC), Los Angeles, California, 22-27 February 2004.
7. S. Blair and Y. Chen, "Resonant-Enhanced Evanescent-Wave Fluorescence Biosensing with Cylindrical Optical Cavities," *Appl. Opt.* **40**, 570-582, (2001).
8. R. W. Boyd and J. E. Heebner, "Sensitive disk resonator photonic biosensor," *Appl. Opt.* **40**, 5742-5747, (2001).
9. E. Krioukov, D.J. W. Klunder, A. Driessen, J. Greve and C. Otto, "Sensor based on an integrated optical microcavity," *Opt. Lett.* **27**, 512-514, (2002).
10. C. Y. Chao and L. J. Guo, "Biochemical sensors based on polymer microrings with sharp asymmetrical resonance," *Appl. Phys. Lett.* **83**, 1527-1529, (2003).
11. R. Grover, T. A. Ibrahim, T. N. Ding, Y. Leng, L. C. Kuo, S. Kanakaraju, K. Amarnath, L. C. Calhoun and P. T. Ho, "Laterally coupled InP-based single-mode microracetrack notch filter," *IEEE Photon. Technol. Lett.* **15**, 1082-1084(2003).
12. C. Manolatou, M. J. Khan, S. Fan, P. R. Villeneuve, H. A. Haus and J. D. Joannopoulos, "Coupling of modes analysis of resonant channel add-drop filters," *IEEE J. Quantum Electron.* **35**, 1322-1331 (1999).
13. A. W. Poon, F. Courvoisier and R. K. Chang, "Multimode resonances in square-shaped optical microcavities," *Opt. Lett.* **26**, 632-634 (2001).

14. Y. L. Pan and R. K. Chang, "Highly efficient prism coupling to whispering gallery modes of a square μ -cavity," *Appl. Phys. Lett.* **82**, 487-489 (2003).
 15. C. Y. Fong and A. W. Poon, "Mode field patterns and preferential mode coupling in planar waveguide-coupled square microcavities," *Opt. Express* **11**, 2897-2904, (2003), <http://www.opticsexpress.org/abstract.cfm?URI=OPEX-11-22-2897>
 16. W. H. Guo, Y. Z. Huang, Q. Y. Lu, and L. J. Yu, "Modes in square resonators," *IEEE J. Quantum Electron.* **39**, 1563-1566 (2003).
 17. H. T. Lee and A. W. Poon, "Fano resonances in prism-coupled square micropillars," *Opt. Lett.* **29**, 5-7, (2004).
 18. C. Y. Fong and A. W. Poon, "Corner-cut square microcavity coupled waveguide crossing," in proceedings of Conference on Lasers and Electro-Optics (CLEO), San Francisco, California 16-21 May 2004.
 19. G. D. Chern, A. W. Poon, R. K. Chang, T. Ben-Messaoud, O. Alloschery, E. Toussaere, J. Zyss and S.-Y. Kuo, "Direct evidence of open ray orbits in a square two-dimensional resonator of dye-doped polymers," *Opt. Lett.* **29**, 1674-1676 (2004).
 20. N. Ma, C. Li and A. W. Poon, "Laterally coupled hexagonal micro-pillar resonator add-drop filters in silicon nitride," to be published in *IEEE Photonics Technol. Lett.*
 21. C. Li, N. Ma, and A. W. Poon, "Waveguide-coupled octagonal microdisk channel add-drop filters," *Opt. Lett.* **29**, 471-473 (2004).
 22. A. Taflov and S. C. Hagness, *Computational Electrodynamics: The Finite-Difference Time-Domain Method* (Boston: Artech House, 2000), Chapter 16.
 23. FullWAVE, Rsoft Inc. Research Software, <http://www.rsoftinc.com>.
-

1. Introduction

Waveguide-coupled circular microdisk and microring resonators have long been attracting considerable attention for channel add-drop filter [1-6] and bio-sensor [7-9] applications. These microresonators are compact size and can partially confine high-Q whispering-gallery modes (WGMs) by total internal reflection (TIR) at the curved microresonator sidewalls. Resonances can be input and output coupled with waveguides only when the cavity wave is wavefront-matched with the waveguide wave. The waveguide coupling can either be lateral [1, 2, 5] or vertical [3, 4, 6]. Lateral coupling has the advantages of monolithic structures and can be fabricated by relatively standard processes. However, it has been recognized that the circular microresonator curved sidewall only allow a short interaction length between the microresonator and the laterally coupled straight waveguides. Such short interaction length imposes a technologically challenging submicrometer air-gap separation constraint between the curved resonator sidewall and the straight side-coupled waveguide sidewall.

In order to increase the interaction length for the lateral coupling between the waveguide and microresonator, racetrack type [10, 11] and a host of polygonal type [12-21] microresonators have been proposed as alternative microresonators. Racetrack type microresonators are comprised of two straight waveguide sections joining with two 180° curved waveguide sections. The two straight waveguide sections allow a long interaction length with the side-coupled waveguides. However, racetrack microresonators have the shortcoming of transition loss due to the modal mismatch between the straight waveguide and the bent waveguide. Moreover, the racetrack 180° waveguide bends and the inner sidewall also introduce waveguide bending loss and surface scattering loss.

Polygonal type microresonators, in the form of square [12-19], hexagon [20], and octagon [21], have the advantage of flat resonator sidewalls. N-bounce ray orbits can be partially confined by TIR at the N-polygonal microresonator flat sidewalls. These N-bounce ray orbits can be wavefront-matched with the input and output-coupled waveguide wave, thus exciting resonances. As compared with racetrack type microresonators, polygonal microresonators do not have the complications of straight-to-bend or bend-to-straight waveguide transition loss, waveguide bending loss, or microring inner sidewall scattering loss. The flat resonator sidewalls are also more favorable for fabrications employing standard microelectronics fabrication processes [20, 21]. However, it has been recognized that polygonal microresonators can have shortcomings of (i) multimode resonances due to different

wavefront-matched ray orbit round-trip lengths, and (ii) cavity loss due to diffraction at sharp cavity corners.

In our previous work [15], we studied high-index contrast laterally waveguide-coupled square microcavities using two-dimensional (2-D) finite-difference time-domain (FDTD) method [22]. Our simulations revealed multimode high-Q resonances that can be identified with modes in k-space. We found that the multimodes are standing-wave resonances due to superposition between open-ray orbits and their back-reflection near the 90° sharp cavity corners. Such standing-wave resonances limit the channel drop efficiency to a mere 25 %, which is unsuitable for channel add-drop applications. Addressing to this issue, we recently proposed the concept of square microcavities with four cavity corners cut at 45° [18]. We referred to this type of tailored square microcavities as corner-cut square microcavities. Our 2-D FDTD simulations of corner-cut square microcavities (laterally coupled with waveguide crossings) suggested nearly traveling-wave resonances that are promising for channel add-drop applications.

Here we report a new concept of modal oscillations in corner-cut square microcavities. We show that open-ray orbits that are 90° -rotated can oscillate between each other upon reflections at the 45° -cut facets, and have the same sense of circulation. Our 2-D FDTD simulations suggest desirable traveling-wave resonances with an optimum corner-cut size, and confirm the proposed modal oscillations. By using Fourier transform (FT) analysis of the simulated mode-field patterns, we quantitatively analyze the modal compositions and periodic modal oscillations for different cut sizes. We also demonstrate fine-tuning of add-drop responses by optimizing the waveguide width.

Section 2 discusses ray optics in 45° -corner-cut square microcavities. Section 3 presents the FDTD simulated spectra of high-index contrast laterally waveguide-coupled corner-cut square microcavities with various cut sizes. We study simulated mode-field patterns and their Fourier transform for quantitative k-space modal composition analysis. We also optimize the add-drop filter responses by fine-tuning the waveguide width. Section 4 concludes this work.

2. Ray optics in 45° -corner-cut square microcavities

2.1 Review of wavefront-matched ray orbits and k-space representation in square microcavities

In order to appreciate the merits of the corner-cut square microcavity design, here we briefly review the essential concepts of wavefront-matched open-ray orbits and k-space modes in square microcavities. One of us previously proposed [13] that square microcavities have 4-bounce closed or open-ray orbits that are TIR-confined at the flat cavity sidewalls, and the orbits can be wavefront-matched with the input-coupled wave upon each round trip. Closed-ray orbits with an incidence angle $\theta = 45^\circ$ always return to the same starting point upon each round trip, enabling traveling-wave resonances. However, open-ray orbits with $\theta \neq 45^\circ$ do not return to the same starting point upon each round trip. Such open-ray orbits can subsequently walk-off and impinge on the orthogonal sidewall, resulting in ray orbits of the same θ but travel backward. Superposition of the forward and backward-propagating open-ray orbits of the same θ can form standing-wave resonances that are, however, undesirable for add-drop applications.

Using physical optics, we can quantitatively model square microcavity modes in k-space [13, 15, 16]. The mode k-vector components in the x and y directions, k_x and k_y , can be discretized in the form $k_x = m_x \pi/a$ and $k_y = m_y \pi/a$, where m_x and m_y are integer number of field extrema along the x and y directions in the cavity, and a is the square microcavity size. The mode ray orbits only propagate in discrete $\theta = \tan^{-1}(m_y/m_x)$ relative to cavity sidewall normal.

2.2 Open-ray orbits oscillations in corner-cut square microcavities

In corner-cut square microcavities, 4-bounce open-ray orbits can impinge on the 45°-cut facets. The reflected ray orbits are then 90°-rotated from the initial orbits and can circulate in the same direction.

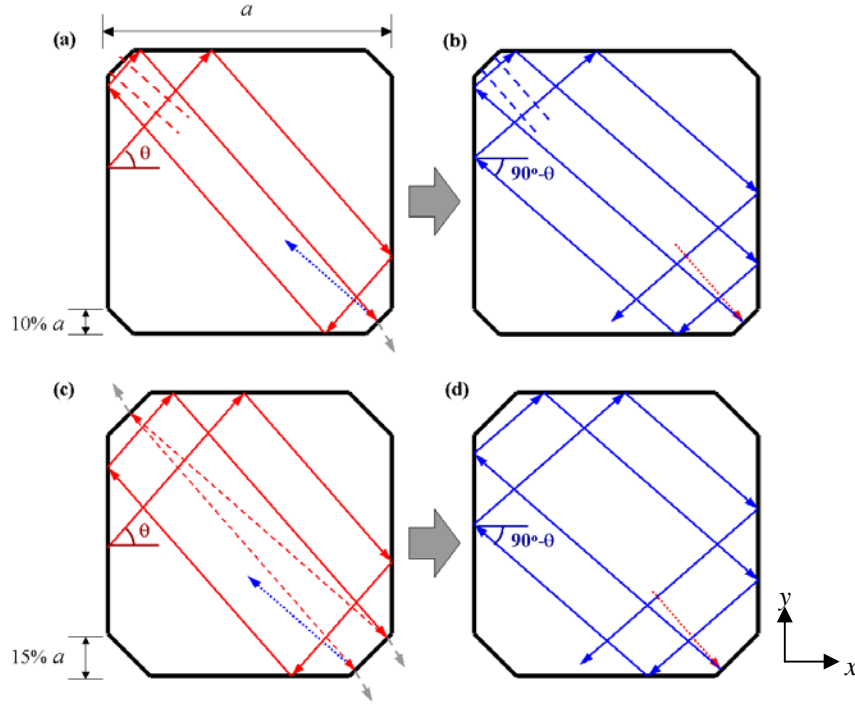


Fig. 1. Ray tracing in a 45°-corner-cut square microcavity with cavity size of a and cut size of (a), (b) $0.1 a$, and (c), (d) $0.15 a$. The wavefront-matched 4-bounce open-ray orbits (red solid) in (a) and (c) have the same $\theta = \tan^{-1}(8/7) = 48.81^\circ$, assuming a $(m_x, m_y) = (7, 8)$ mode. The ray (blue dashed) is partially reflected from the cut facet and partially transmitted (gray dashed). The wavefront-matched 4-bounce open-ray orbits (blue solid) in (b) and (d) are reflected from the cut facet. The ray orbits have an incidence angle of $90^\circ - \theta = 41.19^\circ$, corresponding to a $(m_x, m_y) = (8, 7)$ mode, and preserve the same sense of circulation prior to the reflection.

Figures 1(a) and 1(b) show the ray tracing in a 45°-corner-cut square microcavity with cut size of $0.1 a$. Figure 1(a) shows a wavefront-matched 4-bounce open-ray orbit of $\theta = 48.81^\circ = \tan^{-1}(8/7)$. This ray orbit corresponds to mode $(m_x, m_y) = (7, 8)$. We assumed the modes in corner-cut square microcavities can be approximately represented by the (m_x, m_y) modes. The wavefront-matched 4-bounce ray orbit can end up impinging at the cut facet with a near-normal incidence. Part of the ray refractively escapes with an out-coupling angle according to Snell's law, and the remaining part of the ray is Fresnel reflected. Figure 1(b) shows the wavefront-matched 4-bounce open-ray orbit after the reflection at the cut facet. The reflected ray orbit preserves the same sense of circulation (clockwise) as the initial orbit, and has an incidence angle given by $90^\circ - \theta = 41.19^\circ$, which corresponds to the 90°-rotated mode $(m_x, m_y) = (8, 7)$. Because the corner-cut square microcavities preserve the 4-fold rotation symmetry, the pair of 90°-rotated ray orbits should give rise to degenerate modes.

The cut size can affect the ray dynamics, and thus the cavity loss or the proposed ray orbit oscillations. Figures 1(c) and 1(d) show the ray tracing in a 45°-corner-cut square microcavity with a larger cut size of $0.15 a$. The wavefront-matched 4-bounce open-ray orbit of $\theta = 48.81^\circ$ can be Fresnel reflected back and forth between parallel cut facets along the

microcavity diagonal (Fig. 1(c)) before reflecting into the 90°-rotated ray orbits (Fig. 1(d)). It is conceivable that multiple Fresnel reflections between large-sized cut facets can introduce a relatively large cavity loss. Thus it is of essence to optimize the 45°-cut size in corner-cut square microcavity designs.

We remark that the angle of the corner-cut also matters. Reflections at non-45° cut facets can result in complications with reflected open-ray orbits that are not necessarily degenerate with the initial ray orbits. Here we only focused on the 45°-cut designs.

3. 2-D FDTD simulations of waveguide-coupled corner-cut square microcavities

3.1 Simulation layout

We study the waveguide-coupled corner-cut square microcavity channel add-drop filter concept using a commercial 2-D FDTD package [23]. Figure 2 shows the device schematic. A square microcavity of sidewall-to-side-wall distance a is laterally coupled with two parallel singlemode waveguides of width w . The microcavity and waveguide are separated with an air-gap separation of distance g . The square microcavity corners are cut at 45° from a distance c away from sidewalls. We refer to c as the cut size. The cut end face has a dimension $d = c\sqrt{2}$. In order to simulate high-index contrast silicon-based devices, we chose the device refractive index $n = 3.5$, while the background refractive index is 1.

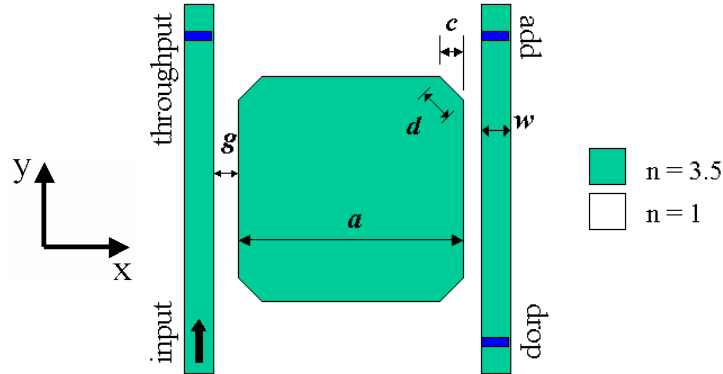


Fig. 2. Schematic of a planar parallel waveguide-coupled corner-cut square microcavity channel add-drop filter.

The detailed simulation parameters are similar to our previous work [15]. A 10-fs Gaussian pulse centered at a vacuum wavelength 1.55 μm is launched into the input waveguide. This pulse covers a wide frequency band of about 31.8 THz (wavelengths from about 1.23 μm to about 2.09 μm). We assumed a slab waveguide fundamental mode profile. We used a 15-nm spatial grid-size and a 0.02-fs temporal step. The spectral resolution is about 0.16 nm – about 0.32 nm (varied by computation time). A perfectly matched layer (PML) of reflectivity 10^{-8} with a thickness of 1.5 μm in the y direction and of 0.5 μm in the x direction is used to absorb stray field at the simulation window boundaries. Virtual detectors are positioned at the throughput, drop and add ports. Mode-field patterns (\mathbf{E} -field) are obtained by launching a continuous-wave (CW) at resonant wavelengths. Here we focused our simulation study on TM polarization (\mathbf{E} -field \perp plane) responses.

3.2 Simulated spectra

Figures 3(a) – 3(e) show the simulated TM-polarized throughput (blue solid), drop (red dashed) and add (green dotted) spectra of parallel waveguide-coupled corner-cut square microcavities of $a = 2.2 \mu\text{m}$ and $c =$ (a) $0 \mu\text{m}$, (b) $0.1 \mu\text{m}$, (c) $0.2 \mu\text{m}$, (d) $0.3 \mu\text{m}$ and (e) $0.4 \mu\text{m}$. We chose a small microcavity size to minimize the number of multimodes. We fixed $w = 0.2 \mu\text{m}$ and $g = 0.2 \mu\text{m}$. Insets show the device schematics. We labeled modes A_0 , B_0 , A_1 , B_1 , B_2 , B_3 and B_4 for the following analysis.

Figure 3(a) shows as a control the spectra of a waveguide-coupled square microcavity as discussed in Ref. [15]. Based on their mode-field patterns, we identify mode A_0 as (6, 9) and mode B_0 as (7, 8). By applying various 45° cut size (Figs. 3(b) – 3(e)), we demonstrate tuning of the resonance add-drop response characteristics (namely drop/add ratio, on/off ratio, coupling efficiency and Q). Below we outline the simulated filter performance characteristics as a function of c .

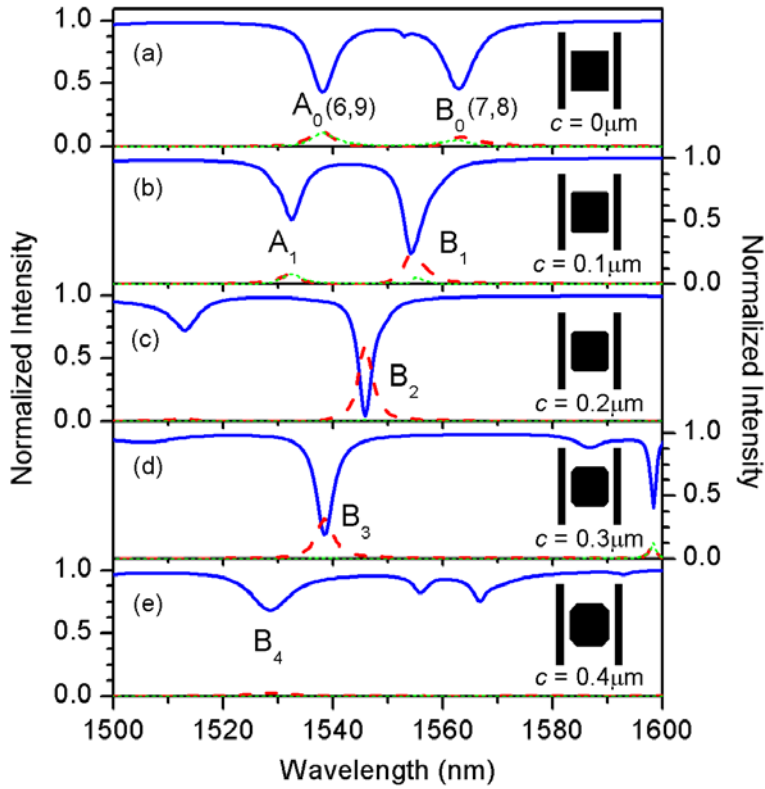


Fig. 3. FDTD simulated TM-polarized throughput (blue solid), drop (red dashed) and add (green dotted) spectra of parallel waveguide-coupled corner-cut square microcavity. $a = 2.2 \mu\text{m}$, $c =$ (a) $0 \mu\text{m}$, (b) $0.1 \mu\text{m}$, (c) $0.2 \mu\text{m}$, (d) $0.3 \mu\text{m}$, and (e) $0.4 \mu\text{m}$. $w = 0.2 \mu\text{m}$ and $g = 0.2 \mu\text{m}$. Insets show the device schematics. We identified mode A_0 as (6, 9) and mode B_0 as (7, 8).

3.3 Add-drop filter analysis

Figure 4(a) shows the drop/add ratio (blue) and on/off ratio (orange) of modes $B_0 - B_4$ as a function of cut size c . We define drop/add ratio as the ratio of on-resonance drop intensity to on-resonance add intensity. A large drop/add ratio suggests that the resonance is dominated by traveling wave and is desirable for add-drop applications. At $c = 0 \mu\text{m}$ (square

microcavity), the drop/add ratio is marginally above 0 dB, which means that the resonance is dominated by standing wave. At $c = 0.2 \mu\text{m} - 0.3 \mu\text{m}$, our simulations suggest that the drop/add ratio can be significantly increased to about 20 dB. This strongly suggests that traveling-wave resonances can be coupled in an optimized corner-cut square microcavity.

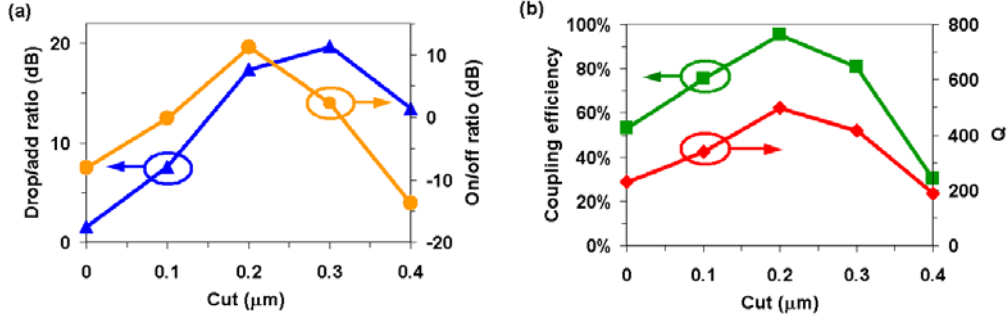


Fig. 4. Analysis of the add-drop filter performance for modes $B_0 - B_4$ as a function of the cut size. (a) Drop/add ratio and on/off ratio. (b) Coupling efficiency and Q.

We define on/off ratio as the ratio of on-resonance drop intensity to on-resonance throughput intensity. A large on/off ratio means a large input coupling and a correspondingly large output coupling to the drop port. At $c = 0 \mu\text{m}$, the on/off ratio is only about -10 dB. At $c = 0.2 \mu\text{m}$, our simulations suggest a significant improvement of about 20 dB in on-off ratio.

Figure 4(b) shows the coupling efficiency (green) and Q (red) of modes $B_0 - B_4$ as a function of cut size c . We define coupling efficiency as the ratio of an estimated on-resonance dip at the throughput to estimated off-resonance throughput intensity. At $c = 0.2 \mu\text{m}$, coupling efficiency of mode B can be optimized to about 95 % (as compared with only about 50 % coupling efficiency at mode B_0), whereas Q can be optimized to about 500 (as compared with $Q \approx 200$ at mode B_0).

As the cut size increases to $0.4 \mu\text{m}$, mode B_4 and other modes are much suppressed (Fig. 3(e)). We attribute this to the potentially increased cavity loss due to the refractive escape at the relatively large-sized cut, as discussed using ray optics in Section 2. It is worth mentioning that as the cut size becomes sufficiently large, we will obtain an octagonal microcavity, whose resonances and add-drop responses have been recently demonstrated on silicon nitride substrates [21].

It is evident that modes A_0 and A_1 do not display similar improvement in filter responses (Figs. 3(a) and 3(b)). Modes A_0 and A_1 have drop/add ratio near 0 dB and are only differed by a spectral shift, suggesting that the improvement due to corner-cut is mode sensitive.

3.4 Mode-field patterns and Fourier transform analysis

In order to gain further insights to the coupled modes in corner-cut square microcavities, we simulate and analyze the steady-state mode-field patterns of modes A_1 , B_1 and B_2 . Figure 5(a) shows the FDTD simulated steady-state electric field pattern of mode A_1 at an arbitrary time. By counting the number of field extrema in the microcavity in the x and y directions, we can identify mode A_1 as $(m_x, m_y) = (6, 9)$ [15, 18]. We also simulated the mode-field pattern time evolution and observed that mode A_1 essentially evolve as a standing wave. We remark that mode A_1 standing-wave field pattern highly resembles that of mode A_0 [15].

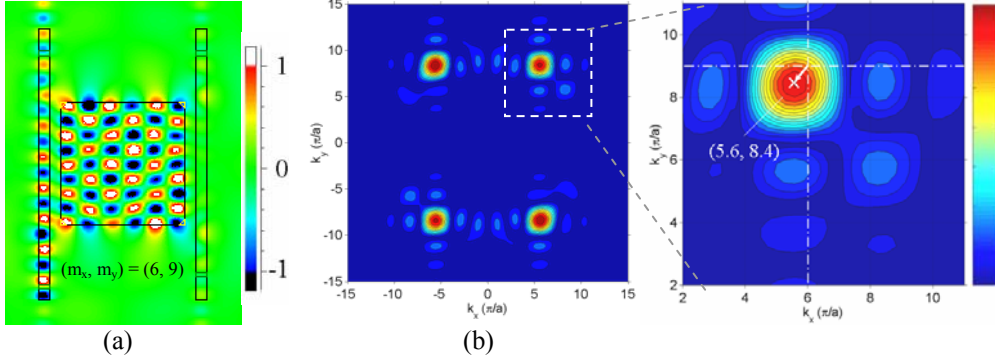


Fig. 5. (a) FDTD simulated steady-state electric-field pattern of mode A_1 . We denote the mode field pattern as $(m_x, m_y) = (6, 9)$. (b) Fourier transform (FT) of the cavity mode-field pattern. Zoom-in view shows the FT peak is shifted from the mode $(6, 9)$.

In order to more quantitatively analyze the modes in k-space, we applied Fourier transform (FT) analysis on the cavity mode-field pattern. Figure 5(b) shows the FT amplitude of mode A_1 field pattern in k-space. The zoom-in view emphasizes on one of the FT peak distributions. It is important to understand that the FT analysis measures the spatial frequency of the mode-field pattern, and thus reveals the modal composition in k-space. In constructing the k-space representation, we neglected the cut facets and assumed a square microcavity.

The zoom-in view shows that the FT components are peaked near the $(6, 9)$ mode (denoted by dashed cross-hair). Because the field extends as a surface wave on the cavity sidewalls (and on the cut facets), the cavity sidewall length effectively exceeds a and thus the k_x and k_y values are expected to be below $m_x \pi/a$ and $m_y \pi/a$. The white arrow denotes such spectral red-shift from mode $(6, 9)$. We remark that such shift from the integer mode numbers is not closely related to the corner cut. A similar shift can be observed for mode A_0 in square microcavities with sharp corners.

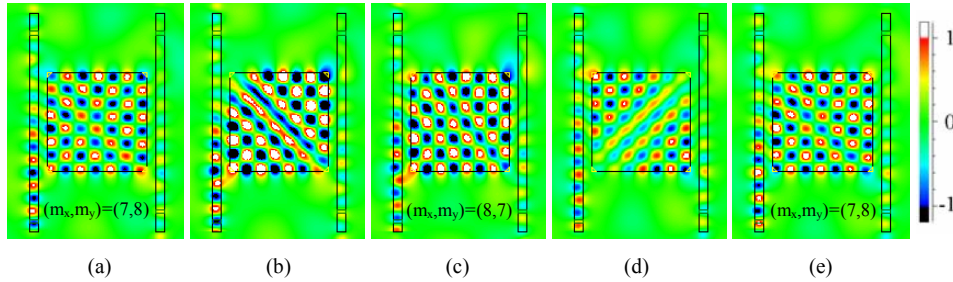


Fig. 6. FDTD simulated steady-state electric-field pattern evolution of mode B_1 . Field patterns are taken at time (a) $t = t_0$, (b) $t \approx t_0 + T/8$, (c) $t \approx t_0 + T/4$, (d) $t \approx t_0 + 3T/8$ and (e) $t \approx t_0 + T/2$. t_0 is an arbitrary time and T is the period. We denote (a), (e) as $(7, 8)$ mode and (c) as $(8, 7)$ mode.

Figures 6(a) – 6(e) show the FDTD simulated steady-state electric-field pattern evolution of mode B_1 from an arbitrary time $t = t_0$ to $t \approx t_0 + T/2$, where T is the period. By counting the number of field extrema in the microcavity in the x and y directions, we can identify $(7, 8)$ mode at $t = t_0$ and $t \approx t_0 + T/2$ (Figs. 6(a) and 6(e)) and $(8, 7)$ mode $t \approx t_0 + T/4$ (Fig. 6(c)). The $(7, 8)$ and $(8, 7)$ modes are 90° -degenerate and have similar field amplitudes. The field evolution suggests that the two degenerate modes oscillate between each other with a relative phase difference of about $\pi/2$. The field evolution also suggests a traveling wave circulating in the clockwise direction. The simulated mode-field pattern evolution thus confirms the concept of modal oscillation as first presented in ray optics in Section 2. We remark that

mode B_0 field pattern evolution essentially comprises (7, 8) mode with only a small contribution from the degenerate (8, 7) mode.

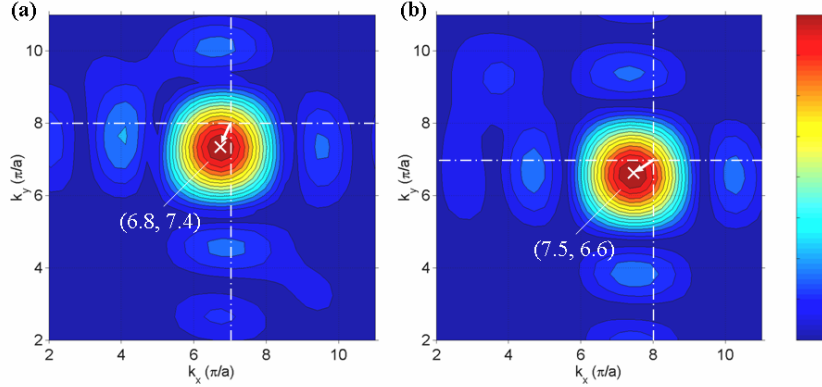


Fig. 7. Fourier transform of mode B_1 field patterns at (a) $t = t_0$ and (b) $t \approx t_0 + T/4$.

Figures 7(a) and 7(b) show the FT of mode B_1 field patterns at $t = t_0$ (Fig. 6(a)) and $t \approx t_0 + T/4$ (Fig. 6(c)). We emphasized on one quadrant of the k -space. As expected, the FT pattern peaks near (a) (7, 8) mode and (b) (8, 7) mode, with similar FT peak counts and widths. The spectral red-shifts from the integer mode numbers are denoted by white arrows.

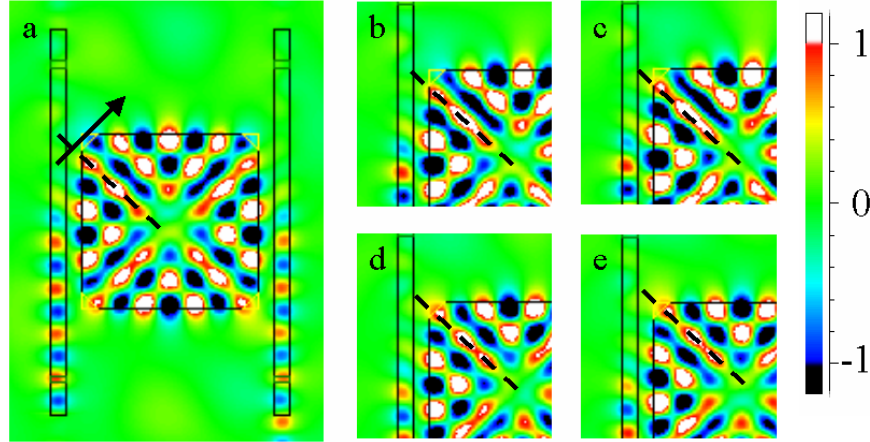


Fig. 8. FDTD simulated steady-state electric-field pattern of mode B_2 . The pattern is vortex-like and travels in a clockwise manner. (a) $t = t_0$, (b) $t \approx t_0 + T/8$, (c) $t \approx t_0 + T/4$, (d) $t \approx t_0 + 3T/8$, and (e) $t \approx t_0 + T/2$. The dashed lines represent a wavefront traveling in the near 45° direction.

Figure 8(a) shows the FDTD simulated steady-state electric-field pattern of mode B_2 at an arbitrary time $t = t_0$. Interestingly, the pattern reveals a vortex-like traveling wave with essentially zero field amplitude at the cavity center. This traveling-wave resonance allows an efficient energy transfer to the drop port (Fig. 3(c)). Figures 8(b) – 8(e) show the detailed mode-field evolution from $t \approx t_0 + T/8$ to $t \approx t_0 + T/2$. Here we only show one-quarter of the microcavity in order to focus on the wavefront propagation. The dashed line indicates the wavefront traveling in near the 45° direction (denoted by the arrow) in a clockwise manner. It is worth mentioning that similar vortex-like mode-field pattern, yet a standing wave, has also been observed in planar waveguide-coupled square microcavities [15].

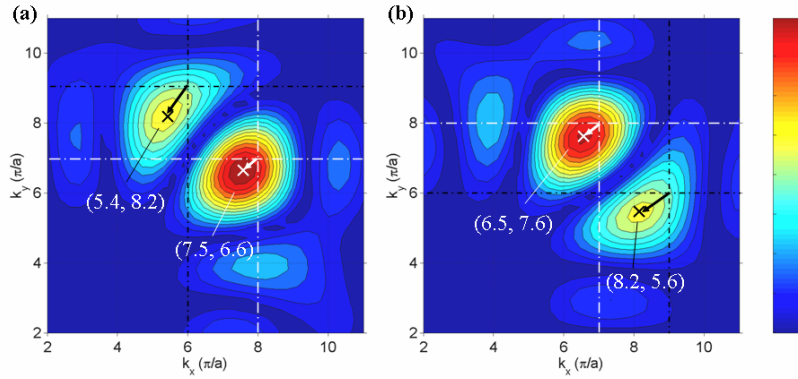


Fig. 9. Fourier transform of mode B_2 field pattern at (a) $t = t_0$ and (b) $t \approx t_0 + T/4$.

Figures 9(a) and 9(b) show the FT of mode B_2 field pattern at $t = t_0$ (Fig. 8(a)) and $t \approx t_0 + T/4$ (Fig. 8(c)). We emphasized on one quadrant of the k -space. At $t = t_0$, the FT pattern reveals that mode B_2 is composed of modes near (8, 7) and (6, 9). Whereas at $t \approx t_0 + T/4$, the FT pattern reveals the modal composition of modes near (7, 8) and (9, 6). Modes (8, 7) and (7, 8) have similar FT counts, and modes (6, 9) and (9, 6) have similar FT counts. We interpret this observation as two parallel modal oscillations: modes (8, 7) and (7, 8) oscillate back and forth (with a relative phase difference of about $\pi/2$), and modes (6, 9) and (9, 6) oscillate back and forth (with a relative phase difference of about $\pi/2$). Surprisingly, modes (8, 7) and (6, 9) and their 90° -rotated modes become degenerate at this corner-cut square microcavity. We refer to this “accidental” degeneracy as corner-cut dependent degeneracy.

3.5 Waveguide-width tuning

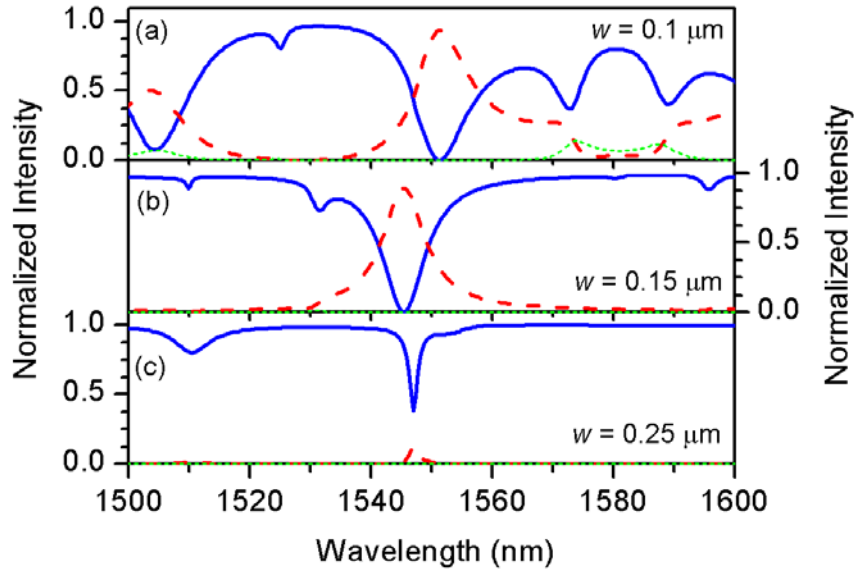


Fig. 10. FDTD-simulated TM-polarized spectra of a parallel waveguide-coupled corner-cut square microcavity of $w =$ (a) $0.1 \mu\text{m}$, (b) $0.15 \mu\text{m}$, and (c) $0.25 \mu\text{m}$. $c = 0.2 \mu\text{m}$, $a = 2.2 \mu\text{m}$ and $g = 0.2 \mu\text{m}$. Throughput (solid blue), drop (dashed red) and add (dashed green).

We further optimize the add-drop filter response by fine-tuning the waveguide width w . Figures 10 show the simulated TM-polarized spectra of a parallel waveguide-coupled corner-cut square microcavity of $w =$ (a) $0.1 \mu\text{m}$, (b) $0.15 \mu\text{m}$, and (c) $0.25 \mu\text{m}$. We fixed $c = 0.2 \mu\text{m}$, $a = 2.2 \mu\text{m}$ and $g = 0.2 \mu\text{m}$. It is evident that $w = 0.15 \mu\text{m}$ exhibits desirable nearly singlemode add-drop filter responses. Our simulations of w tuning suggest an optimum coupling efficiency exceeding 99 %, a drop/add ratio of about 23 dB, and an on/off ratio of about 24 dB. We remark that the $w = 0.15 \mu\text{m}$ slab waveguide (with index $n = 3.5$) has a mode propagation angle near 45° , and thus possibly favorable for phase matching with 4-bounce modes [15].

4. Conclusion

In summary, we examined the recently proposed planar waveguide-coupled corner-cut square microcavity channel add-drop filters, using ray tracing and FDTD method. Ray tracing reveals that 4-bounce open-ray orbits that are 90° -rotated can oscillate between each other upon reflections at the 45° -cut facets. These corner-reflected ray orbits can travel in the same sense of circulation, and thus potentially give rise to traveling-wave resonances that are desirable for add-drop applications.

Our FDTD simulated spectra suggest that the corner-cut design can significantly improve the planar waveguide-coupled square microcavity add-drop filter responses. We analyzed the cavity mode-field patterns in real-space and in Fourier-transformed k -space and confirmed the concept of modal oscillations in corner-cut square microcavities. Interestingly, vortex-like traveling-wave mode-field patterns are observed with the optimum corner-cut microcavity.

Lastly, our simulations suggest that the add-drop filter responses can be optimized by fine-tuning the coupled-waveguide width. By properly tailoring the square microcavity shape, in particular the microcavity corners, we believe that square microcavities with optimum corner-cut designs are promising building blocks for high-index contrast integrated photonic circuits.

Acknowledgement

The work described in this paper was substantially supported by grants from the Research Grants Council and from the University Grants Council of the Hong Kong Special Administrative Region, China (Project No. HKUST6166/02E & HIA01/02.EG05). C. Y. Fong's studentship was partially supported by a grant from the Institute of Integrated Microsystems of The Hong Kong University of Science and Technology (Project No. I2MS01/02.EG07).